

Different initial density turbidite sediments with coarse grain injection and their corresponding flow pattern: Additional insights from numerical simulation in a study case of South China Sea

Chao Fu ^a, Xinghe Yu ^{a,*}, Yulin He ^b, Jianqiang Liang ^b, Zenggui Kuang ^b

^a School of Energy Resources, China University of Geosciences, Beijing, Beijing, 100083, China

^b Guangzhou Marine Geological Survey, Guangzhou, 510760, China

ARTICLE INFO

Article history:

Received 10 September 2018

Received in revised form

29 November 2018

Accepted 4 December 2018

Available online 7 December 2018

Keywords:

Turbidite sedimentation

Subcritical turbidity flow

Numerical simulation

Deep-water slope

Flow pattern

ABSTRACT

The work presents the sedimentology and depositional results of the turbidity flow from Miocene to Pliocene along the North Slope of South China Sea (SCS). The integration of the core-log-seismic data has enabled us to clarify turbidity flow with different density and characterize their corresponding seismic geomorphic sedimentation. Based on the differences between the initial density and the later, we classified the turbidity flow into two types, namely: low- and high-density flow with coarse grain injection. According to the hydrodynamic numerical simulation results, we constructed different subcritical turbidity flow models with various density and rebuilt the depositional pattern along the slope. As to the numerical simulation model, we introduced the erosion rate into the classical full Reynolds-averaged N-S (RANS) equation, which is suitable to the deep-sea slope area. Through comparison of the above simulation models, the results show that the high-density turbidites with coarse-grained injection are mostly developed with lower vertical erosion rates and higher lateral abrasion rates. They are characterized with multi-branched and lobe-shaped sedimentary volumes, while low-density turbidites with coarse-grained injection are characterized with higher vertical erosion rates and lower lateral abrasion rates. And this kind of turbidites can generate single-branched and banding deposits. In addition, the fluctuating sea levels and the varying topographies are important to influence the subcritical turbidity flow models in the deep-water slope.

© 2018 Chinese Petroleum Society. Publishing Services by Elsevier B.V. on behalf of KeAi. This is an open access article under the CC BY-NC-ND license (<http://creativecommons.org/licenses/by-nc-nd/4.0/>).

1. Introduction

Turbidity flow deposits developed at the most of continental margin serve as the favorable reservoir to petroleum and gas hydrate exploration (Milkov and Sassen, 2001). The channel-levee-lobe system building and the turbidity channel avulsion are mostly determined by the turbidity current flow pattern (Picot et al., 2016). However, the complex hydrodynamic settings and the dramatic topographic changes at the slope break often lead to many types of turbidite sediments, which make it a big challenge to investigate the underlying formation mechanism of these sediments.

The former studies had classified the turbidity flow into several types based on their flow patterns from the results of physical

experiments (Garcia and Parker, 1993; Woods and Bursik, 1994; Stow et al., 2009; Kane et al., 2010; Postma et al., 2014), and from the field outcrop descriptions (Walker and Harms, 1970; Shanmugam et al., 1993; Gardner et al., 2003; Mutti et al., 2003; Surpless et al., 2009; Flint et al., 2011). But because of the complex sedimentation process along the slope, such as nearby canyon collapsing, slump flowing and bottom current reworking etc. (Mutti et al., 2003; Dott, 1963; Lowe, 1982; Gong et al., 2016), the primary structure and distribution would be reworked. The former study methodologies cannot meet the subcritical turbidity flow developed along a gentle slope with complex hydrodynamic settings (Boulay et al., 2005; El-Gawad et al., 2012; Ma et al., 2015). Nevertheless, the high erosion rate, together with the unstable channel settings lead by the unidirectional channel migration (UCM), all seem to weaken the reliability of these flow models (Gong et al., 2016). Thus, it is necessary to build a corresponding flow pattern, which can simulate the progress from triggering to depositing.

* Corresponding author.

E-mail address: billyu@cugb.edu.cn (X. Yu).

The main questions come to how the turbidity flow evolve when mass coarse-grained injection, and what is the various the subcritical turbidity flow develop pattern. [Marisset et al. \(2009\)](#) and [Picot et al. \(2016\)](#) both proposed the sedimentary parameters and the methodologies based on seismic-log-core data. Meanwhile, [Iverson \(1997\)](#) and [El-Gawad et al. \(2012\)](#) described the turbidity flow patterns based on physical experiments and numerical simulations. Per study are mostly using highly resolved numerical models known as Direct Numerical Simulation (DNS) or simulate turbidity currents with CFD software Flow-3-DTM ([Iverson, 1997; El-Gawad et al., 2012](#)). But they merely considered the flow patterns with less coarse-grained injection and ignored the erosion rate calculation and density difference in the slope break area. In this paper, based on the traditional flow model, the erosion rate is introduced into the flow rate equation, and the subcritical turbidity flow model is developed with detailed formulations. The proposed model shows a good agreement with the interpretation of seismic data and different types of turbidity deposit distribution.

Until now, many flow patterns had been pointed out for turbidity flow. [Huang et al. \(2007\)](#) simulated the exchanging progress between turbidity flow and seabed sediment by using the turbulence $k-\epsilon$ model. [Postma and Cartigny \(2014\)](#) put forward that the subcritical state of turbidity flow is most prone to subsiding. However, few works have been implemented with regard to a flow model, which takes into account the coarse-grained injection along the slope at the break area. Especially for the slope break, considering the fluctuation of palaeo-topography, they all play an important role on the turbidity flow development. Therefore, the relationship between different turbidity flow concentration and their corresponding sedimentary architecture distribution, flow pattern, impact factors should be clarified ([Picot et al., 2016](#)). [Mulder and Alexander \(2001\)](#) considered that the cohesive turbidities flow can be divided into two types as the difference of clay content. [Hodson and Alexander, 2010](#) also pointed out clay content have relationship with densities, especially for study area as [Li et al. \(2017\)](#). Meanwhile, by investigating the turbidity flow with different densities, an important contribution from this work is to enhance the understanding of the relationship between the detailed deposition morphology and its corresponding control factors, and to allow for a better prediction of the turbidity reservoir at the slope area in the future works.

This paper is organized as follows: first, geological settings, methodologies and data preparation are presented to give a background of the study. Next, different types of turbidity flow are identified through litho-facies description and seismic-log-core integration analysis. Then, the sedimentary characterization of different types of turbidite sediments and results of the proposed subcritical flow model obtained from numerical simulation are presented. Finally, the impact factors to the deposition model are discussed at the end.

2. Geological settings

The study area is located in the deep sea sedimentary area of the Baiyun Sag in the southern Pearl River Mouth Basin (PRMB), the central section of South China Sea (SCS) northern slope. The longitude ranges from $115^{\circ}10''$ to $115^{\circ}20''$ ([Fig. 1](#)). The PRMB is a Cenozoic sedimentary basin, which has experienced three tectonic phases or stages after the Paleogene ([Fig. 2](#)), namely the rifting stage during the Paleocene to the early Oligocene, the transition stage in the late Oligocene, and the depression stage during the early Miocene to the Quaternary ([Xie et al., 2014; Clift et al., 2015; Han et al., 2016](#)). Turbidity dispositions were mainly developed at Yuehai formation and Wanshan formation, which is development during Miocene ([Gong et al., 2016](#)). The Yuehai Formation was

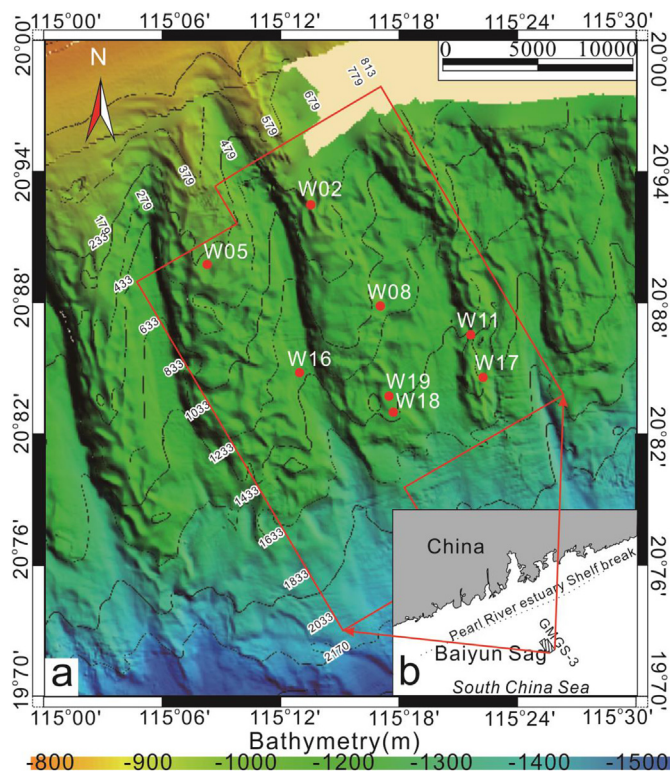


Fig. 1. Study location of the area. (a) Bathymetry across the break is in the north slope of South China Sea. The water depth ranges from -800 m to -1500 m. (b) Location of Baiyun Sag.

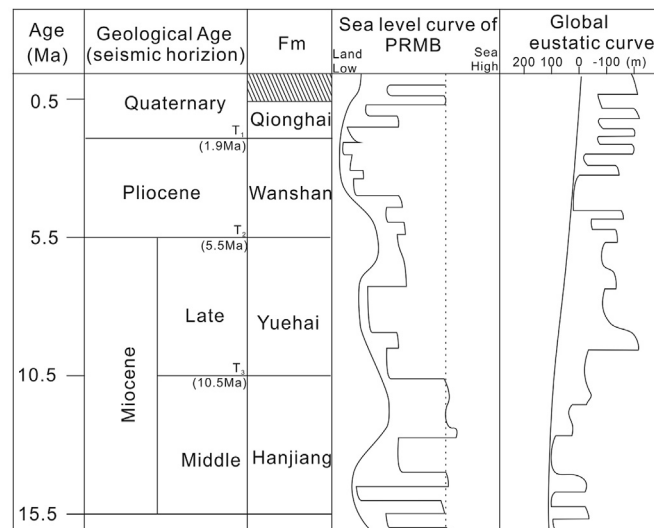


Fig. 2. Stratigraphic description and its corresponding sedimentary environment. The middle two columns represent the sea level curve of Pearl River Mouth Basin (PRMB) ([Han et al., 2016](#)) and the global eustatic curve. Sequence framework (T_0 , T_1 , T_2 , and T_3) after the Paleogene is established based on the change of sea levels.

developed during late Oligocene–Miocene (10.5–5.5 Ma), when a large-scale tectonic movement occurred in the SCS (which was called the ‘Baiyun’ movement), making the Pearl River estuary shelf-break drifted northwards and becoming the depositional center. The Wanshan Formation was mainly developed during the late Pliocene (5.5–1.9 Ma). ([Steinke and Groeneveld, 2010; Han et al., 2016](#)).

Han et al. (2016) proposed that the sea level in the SCS had been rising continuously since the late Miocene, and combining with the increasing of the slope dip angle. At that time, the degree of transgression in the northern SCS was enhanced (Fig. 2), and the progradation of the shelf delta in the Pearl River estuary was limited. At the same time, there was a significant northward migration in the sedimentation process. The early period of the third-order eustatic cycle only reached the extent of the continental shelf. During the early stages, coarse-grained sediments were mainly deposited in the Panyu low-uplift area of the outer shelf. (Boulay et al., 2005; Zhou et al., 2015).

The turbidity flow depositions were mostly developed along the toe of the slope. The main sedimentary types include: the tractive current deposition caused by inter-wave, the slumping block deposition caused by apron sliding, and the current reworking deposition caused by ocean current, namely North Pacific intermediate water and North Pacific Deep water (Clift et al., 2015).

The modern ocean circulation in the South China Sea is mainly controlled by the semi-enclosed basin physiography and can be divided into seasonal surface-water circulation (<350 m), intermediate water circulation resulting from the North Pacific intermediate water (NPIW; 350–1350 m), and the deep-water circulation associated with the North Pacific deep water (>1350 m). Considering that along-toe of the slope (contour) currents generally involve significant water mass in certain bathymetric depth ranges and persist for a very long time interval, bottom currents associated with the intermediate water circulation resulting from the NPIW (NPIW-BCs) most likely have a profound influence on the development of the studied unidirectional migrating deep-water channels that are located primarily in water depths ranging from 500 to 1300 m.

3. Methodologies and data preparation

Cores, wire-line logs and 3D seismic data (in the year of 2007 and 2015) are the main sources for the study obtained by Guangzhou Marine Geological Survey (GMGS). Four core samples are collected along the slope from W17 and W18 (the well sites as shown in Fig. 1).

The pseudo-three dimensional (3D) survey data used in this paper were acquired by GMGS during 2008–2009, with the average frequency of 65 Hz and the sampling interval of 1 ms, for an area of approximately 15 km × 25 km. To accurately describe the sedimentary volume, the time window is set at 3 ms per slice. The seismic compound attributes (including the mean-square-foot amplitude (RMS), instantaneous frequency amplitude (IF), and instantaneous phase amplitude (IP)) were prepared in the former time period to adequately reflect the saturation and other physical properties of the deep-water turbidity flow.

3.1. Sedimentary parameter statistical method

In order to simulate the subcritical turbidity flow, the architectural parameters of different types of turbidity flow are needed. Thus, improved method as reported in Marsset et al. (2009) and Picot et al. (2016) are used, which includes the following parameters: (1) Channel length (CL); (2) Distance to avulsion point (DA); (3) The number of avulsion point (NbA); (4) The number of slump deposition (NbS); (5) The number of intersection point (Nbl); (6) Bifurcation angle of branches. The parameters are distinguished by the RMS attribute time slice, with the time window of 60 ms from the layers of Yuehai Formation to the layers of Wanshan Formation. The RMS attribute is also extracted with an interval of 10 ms. These parameters are presented on the diagrams in the chronological order with the help of ArcGIS® software.

3.2. Numerical simulation method

3.2.1. Flow rate calculation

A three-dimensional (3D) numerical model of turbidity current evolution was given by the full Reynolds-averaged Navier-Stokes (RANS) equation (Georgoulas et al., 2012; Nasr-Azadani and Meiburg, 2011). After combining the revised turbulence model given by Huang et al. (2007), the governing equation of the flow field can be written as:

$$\frac{\partial u_i}{\partial x_i} = 0$$

$$\frac{\partial u_i}{\partial t} + \frac{\partial (u_i u_j)}{\partial x_j} = -\frac{1}{\rho_n} \frac{\partial P}{\partial x_i} + \frac{\partial}{\partial x_j} \left(2(\nu + \nu_t) S_{ij} - \frac{2}{3} k \delta_{ij} \right) + \Delta \rho g_i \quad (1)$$

Where $i = 1, 2, 3, j = 1, 2, 3$, x_1 is the direction of turbidity flow along the slope, x_2 is perpendicular to x_1 (along the slope break), and x_3 is the direction of gravity.

P is the overburden pressure. u_i (or u_j) is the corresponding velocity component of the turbidity flow in x_i (or x_j) direction.

ρ_n is the density of the turbidity flow, where n denotes the number of simulations. The density changeable has a linear relationship with its grain size: $r_n = 0.7351\rho_n + 0.0298$. $\Delta\rho$ is the density difference between the turbidites grain size and the one after coarse-grained injection. ν is viscosity of the turbidity flow (the value is nearly $10^{-6} \text{ m}^2\text{s}^{-1}$). g_i is the vertical gravity acceleration ($g_1 = g_2 = 0, g_3 = g$). δ_{ij} is Kronecker delta function ($i = j, \delta_{ij} = 1; i \neq j, \delta_{ij} = 0$).

The average strain-rate tensor is given by:

$$S_{ij} = \frac{\partial u_i}{\partial x_j} + \frac{\partial u_j}{\partial x_i} \quad (2)$$

Following the derivations in Appendix A, by solving Eq. (1), we get the relationship between the velocity u and its corresponding density. Then, based on the initial density of the turbidity flow at each simulation time n ($n = 1, 2, 3 \dots$), the flow rate and the time step are determined so that the flow progress of turbidity flow with different grain size can be simulated.

3.2.2. Erosion calculation

Considering the erosion of turbidity channel, the instability of channel wall at the toe of the slope, and the impact of the coarse-grained injection into the sedimentary gravity flow, we introduce an erosion calculation into the traditional numerical simulation of the disposition progress (Iverson and Lahusen, 1993).

Due to the complex sedimentary settings at the toe of the slope, the lateral abrasion and vertical erosion is varying during the simulation (El-Gawad et al., 2012). We convert the mixed density into the mixture ratio (N_{mass}) as follows:

$$N_{\text{mass}} = \frac{nV}{1 - nV} \frac{\rho_n}{\Delta\rho} \quad (3)$$

n is the ratio of coarse-grained content, and the V is the volume of all the turbidities is in the canyon area. We revised turbulence model of Huang et al. (2007) by introducing an erosion parameter N_{fric} . Based on Iverson's (1997) erosion model, this work also uses a parameter, N_{fric} , to calculate the Bingham number, which is represented for the vertical erosional capacity of different grained turbidities to the canyon walls. N_{fric} is given as:

$$N_{fric} = \frac{nV}{1-nV} \frac{N_{mass}(r_n - n\Delta r)g \tan \phi}{v} \quad (4)$$

Δr is the difference between the maximum and the minimum grain size in the turbidities. Φ is the failure envelope angle (as shown in Table 1). $N_{mass}(r_n - n\Delta r)g \tan \phi$ is the bed failure envelope for different density turbidity flows. The increase of the density can cause the increase of failure envelope angle (as illustrated in Fig. 3-a to c). Combining the flow rate u_i (Eq. (1)) with the erosional capacity (Eq. (5)), the erosion rate along the slope can be simulated.

Assuming that all the substances caused by erosion is injected into the turbidity flow in an ideal condition, and the turbidity flows are eventually formed into mixed flow eventually. The density of the mixed turbidity flow is a transient variable, which can be shown as the following integral:

$$\int_0^L \frac{\partial \Delta r}{\partial x_1} dx_1 = \int_0^L \frac{\partial (N_{fric} u_i)}{\partial x_1} dx_1 \quad (5)$$

Where L is the total length of the turbidity flow. Substituting Eq. (3) and Eq. (4) into Eqs. (1) and (5) along the slope, and apply an iterative calculation, we finally get the turbidity flow model of the development progress corresponding to different types of turbidity sediments. Detailed derivation can be found in Appendix B.

3.2.3. Flow pattern analysis

The previous study (Huang et al., 2007) introduced a Froude number (Fr) into the flow pattern analysis, which can reflect the sedimentary parameters including the ratio between channel width and depth, the simulation of the turbidity flow, and the stability of the channel levee etc. At the upstream slope, the initial velocity (u) is relatively fast and the Fr number is greater than 1. This kind of flow pattern can also be named as the supercritical turbidity flow. With the declination of the dip angle, the flow velocity also decreases with the Fr number. Once the Fr number is below 1, and this kind of flow is called subcritical, which may cause the sediments deposition and the lobe formation (Huang et al., 2007; Shanmugam et al., 1993). Richards (1994) pointed out that the distribution of the sedimentary architecture, especially the bifurcation angle of the branches and the number of avulsion points are mainly dominated by the location of subcritical turbidity flow. Four steps are used in this work to get the flow pattern (Fr number) in different types of turbidity sediments:

- (1) The simulated sediments deposition pattern is used to calculate the fraction of each grain class, and the velocity of turbidity flow, as well as the thickness of sediment volume.
- (2) Considering the dip angle change during the Miocene, we reconstruct the palaeo geomorphology of different geological

times since the 11 Ma (Firstly, we get the seismic data in-depth with its geological time calibration based on the document of Clift et al. (2015), and we get the isochronous surface, based on the contraction of seismic package. Then, with the help of Petrel software, we get the geomorphology.). By combining the seismic profile interpretation and the high-density injection statistical analysis, we also take into account the direction of turbidity flow and its nearby high-density injection in our simulation. (3) The input density data are based on the core sample description as listed in Table 1. In this work, the turbidity flow is classified into three types based on the density and density, namely, the high-density flow ($\rho = 2.5 \times 10^3 \text{ kg m}^{-3}$, $r = 2^{-3} \text{ m}$), the moderate density flow ($\rho = 2.0 \times 10^3 \text{ kg m}^{-3}$, $r = 2^{-6} \text{ m}$), and the low-density ($\rho = 1.5 \times 10^3 \text{ kg m}^{-3}$, $r = 2^{-9} \text{ m}$). (4) Simulation results from this run gives the distribution of the subcritical turbidity flow.

3.2.4. Boundary conditions

Solution of the above equations requires specification of physical boundaries of the computational domain. During the flow process, all the inlet, velocity, sediment concentration, and the turbidity current thickness can be input as a constant values. While when the Fr number decreasing below 1, zero gradient extrapolation is used and mass flux balance is checked for velocity correction. 1) The surface between the bottom flow and the density turbidities flow can be used boundary conditions to describe the momentum of sediment in the bed (Grachev and Fairall, 2001). 2) To the boundary between the turbidities flow and the bottom basement, we take consider of the substances caused by erosion is injected into the turbidity flow. Then we use the Exner equation to simulated the basement dip change:

$$(1 - \lambda_n) \frac{\partial Y}{\partial t} + \frac{\partial q_s}{\partial x_1} = 0 \quad (6)$$

λ_n is porosity of bed material; Y is the evaluation height from the lowest level, which can be calculated by x_1 in the equation as Fig. 7 q_s is the volume of sediment provided, it would be given as it change with the time step.

4. Identification of different types of turbidite sediments

4.1. Litho-facies description

According to the litho-facies described in the core, different types of turbidite sediments are identified. The core intervals in the Shenhua new drilling area suggest that density of the sediment ranges widely, from mud to coarse sandstone (Table 1). In this study, the “fine-grained sediments” are mainly mud and silt, and

Table 1
The litho-facies classification and descriptions.

No.	Code	Litho-facies name	Density (kgm ⁻³)	Main lithology	Failure envelope angle(ϕ)	Sedimentary structure and facies identification
L.1	Mcg	Graded bedding silty mudstone	1.5–1.8	Mudstone and siltstone	10°–30°	Graded bedding and wavy bedding; corresponding to the Tb and Tc in Bouma sequence;
L.2	Fcg	Graded bedding fine sand	2.0–2.5	Siltstone and fine-grained sandstone	>30°	Graded bedding and Wavy bedding; corresponding to the Ta and Tb in Bouma sequence;
L.3	Fd	Deformation structure fine sand	> 2.5	Siltstone and fine-grained sandstone	None	Silty deformation; Geschiebe formation at the bottom; contemporaneous deformation structure;
L.4	Fcw	Wavy bedding silty- mudstone	1.5–1.8	Mudstone and siltstone	< 10°	Wavy bedding; abundant foraminifera at the bottom
L.5	Fc	Mixed bedding fine sand		Mudstone and siltstone	10°–30°	Mixture of the mud turbidites and sandy turbidites, graded bedding;

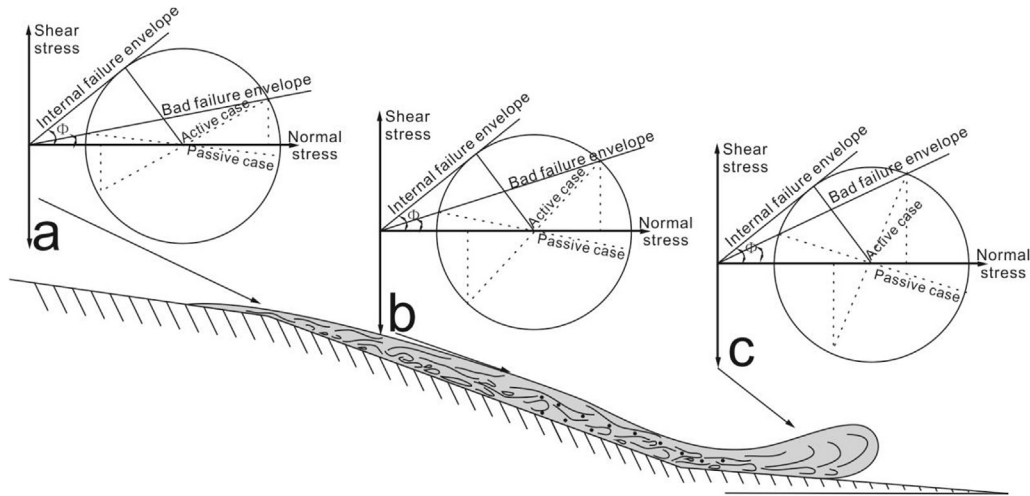


Fig. 3. The erosion progress during the turbidity flowing. (a) is the erosion resistance capability along the slope. The dip angle is selected as 10° at the upstream (Crossline 233–1433) and 5° at the downstream (Crossline 1433–2170). The arrow above the thalweg deposition represents the coarse-grained injection progress. From the left to the right are: the initial mixture turbidity flow, the coarse-grained injection caused by vertical erosion, and the coarse-grained injection caused by lateral abrasion. Substitute the shear rupture angle Φ into Eq. (5), we can get the erosion rate of different directions along the slope. e is the vertical erosion rate of the basement along the slope and f is the lateral abrasion rate. As the equation shown, the vertical erosion rate is the multiply of the fluid rate, calculated above, and the lateral abrasion rate can be get as equation (4).

“coarse-grained sediments” are mainly sand (and sometimes even silt). The sedimentary structures include: traction current structure, deformation structure and graded bedding structure. According to the sedimentary process of gravity flow and the bed-scale of sedimentary structure, this work divides the litho-facies into five class, namely L1–L5 (see Fig. 4-a to e) (Bouma et al., 1962; Postma et al., 2014). The descriptions of each type of litho-facies are listed below follows:

- (1) The litho-facies of graded bedding silty mudstone (L1 in Fig. 4-a) is mainly composed by fine-grained siltstone. The observed structure is paralleled lamina at the bottom and spiral lamina at the top, which corresponds to the layers of T_b and T_c in the Bouma et al. (1962) sequence.
- (2) Graded bedding fine sand (L2 in Fig. 4-b) mainly consists of coarse-grained sandy sediments, and can be characterized

with the coarsening-upward lithological sequence. This kind of litho-facies corresponds to the layers of T_a and T_b in the Bouma et al. (1962) sequence. It can be interpreted as the coarse-grained turbidity flow.

- (3) Fine sand with deformation structures are shown in L3 of Fig. 4-c, which can be explained by the collapse sedimentation caused by channel migration (Wu et al., 2011).
- (4) L4 in Fig. 4-d mainly consists of fine-grained siltstone facies. It is characterized with a series of high-angle interlaced wave bedding, which can be considered as the modification structure caused by the latter bottom water (Gong et al., 2016).
- (5) L5 in Fig. 4-e is mainly the heterogeneous mixture with the coarse-grained silty turbidites at the bottom, fine-grained muddy turbidites at the top, and the mixed transition phase in between.

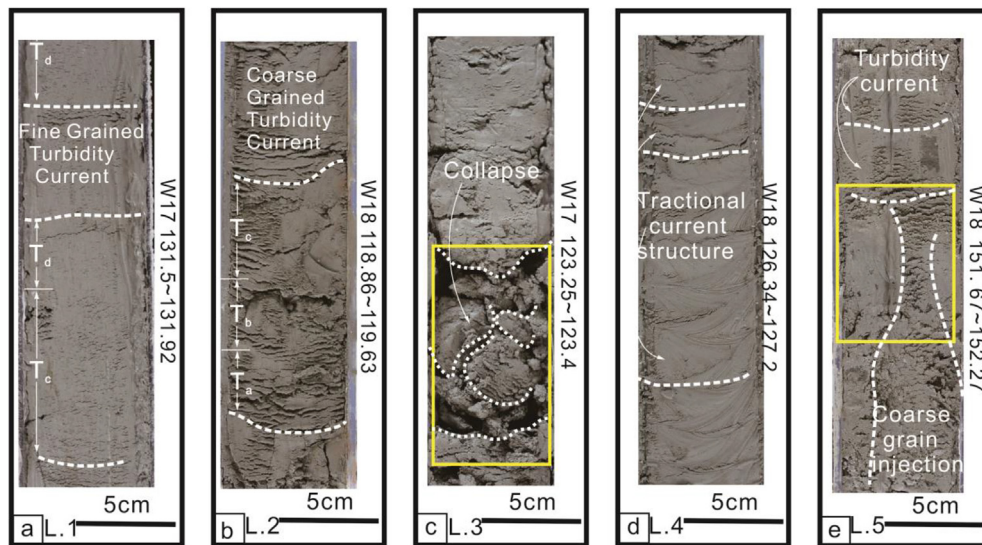


Fig. 4. Classification of core samples: (a) Graded bedding silty mudstone (Mcg). It corresponds to T_c and T_d of Bouma Sequence; (b) Graded bedding fine sand (Fcg). It corresponds to T_a and T_b of Bouma Sequence; (c) Deformation and crumpled structure fine sand (Fd); (d) Climbing ripples silty-mudstone (Fcw); (e) Mixed bedding fine sand (Fc). The white dotted lines depict the heterogeneous mixture of the turbidites with different densities.

By comparing the core samples as described in Table 1, it indicates that turbidity flow in the study can be divided into two types, namely fine-grained and coarse-grained. The heterogeneous mixed flow in L5 reflects the coarse grain injection during the flowing process.

4.2. Seismic facies identification

Through studying 3-D seismic volume in the GMGS-3 drilling area, the seismic facies are divided into four types (Sf.1–Sf.4) (Fig. 5). Combining with the calibration of log and core data (Fig. 7 core sample characteristic), the seismic facies are described in this paper in the aspects of deposition morphology and reflection amplitude (Roberts et al., 1996; Postma et al., 2014).

The first kind of filling facies (Sf.1) is characterized with the high-amplitude reflections at bottom of the filling (Fig. 5-a), which can be explained as the thalweg deposit of turbidity channel (Wang et al., 2014). The inner events are superposed upward horizontally. The facies show that the fillings have low-amplitude inner events and the distinct reflection boundary. With the help of logging curve and the corresponding core from W18, Sf.1 can be identified by the seismic trace beside the well at a depth of 20 m beneath the sea-floor. It presents a high GR value ($API \approx 60-120$) and fine-grained continuous litho-facies of L1. Therefore, this kind of filling facies can be interpreted as the fine-grained turbidity flow deposition. (Salimullah and Stow, 1995).

Another kind of filling facies (Sf.2) is characterized with the high-amplitude inner events and the indistinct reflection boundary (Fig. 5-b). The inter events are also superposed upward horizontally the same as Sf.1. With the help of logging curve and the corresponding core from W17 at a depth of 80 m beneath the seafloor, it

presents a low GR value ($API < 60$) and fine-grained continuous litho-facies of L2. Thus, by comparing with the seismic facies analysis, this kind of filling facies can be interpreted as the coarse-grained turbidity flow deposition.

Sf.3 (Fig. 5-c) has a mound-like reflection boundary and the chaotic inner events. The observation of the logging curve from W18 at a depth of 50 m beneath the seafloor shows a finger shaped high value area of the GR curve. And the L3 litho-facies are mainly developed from the core analysis. This can be interpreted as the coarse-grained slump deposition. Sf. 4 (Fig. 5-d) is characterized with the low-amplitude reflections and continuous seismic events. The corresponding logging curve is almost smooth and its GR value is relatively high ($API > 90$), which can be interpreted as the hemipelagic or the fine-grained deposition.

5. Seismic geomorphology and turbidites channel recognition

In this study we can distinguish the deep-water channel with the RMS attribute maps in seismic slice within 2000 ms (Fig. 6a) and 2500 ms (Fig. 6b), with the RMS attribute values. It is possible to determine the distribution of coarse-grained sediments, such as the turbidity flow channel, the canyon wall collision and the lobe, base on the area with high RMS-attribute values. The attribute map shown in Fig. 6 a and b is the get in various depth, which shows different density as Table 2 shown.

With the above seismic facies identified and the seismic slice shown, Channel C is mainly filled with coarse -grain sediment. Down along with the slope are less prone to bend (Fig. 6-b). And measuring the distance to the slope break, the bifurcation point located at the half of channel. Channel D is also filled with fine

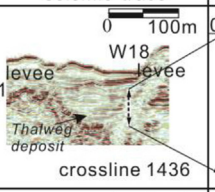
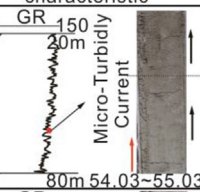
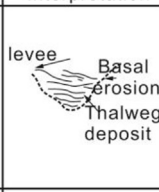
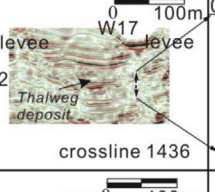
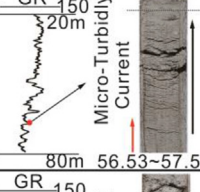
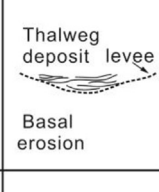
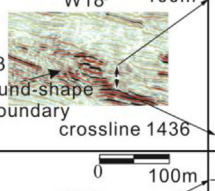
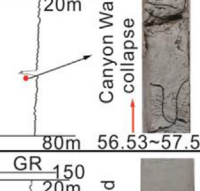
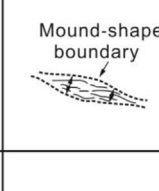
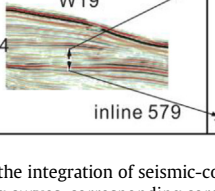
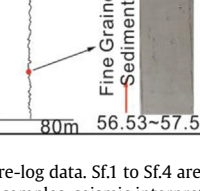
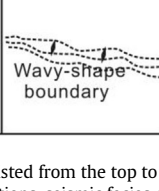
	Borehole seismic trace	Core sample characteristic	Seismic interpretation	Seismic face characteristic(RMS value)	Responding sediment facies
a	Sf. 1 			Discontinuous seismic event Low-amplitude reflection Distinct filling-shape seismic boundary (10000–12500, Ave. 11000)	LOW DENSITY TURBIDITY CHANNEL
b	Sf. 2 			Discontinuous seismic event High-amplitude reflection Undistinct filling-shape seismic boundary (10000–12500, Ave. 11000)	HIGH DENSITY TURBIDITY CHANNEL
c	Sf. 3 			Discontinuous seismic event High-amplitude reflection Distinct mound-shape seismic boundary (7500–12500, Ave. 10000)	LEVEE & CANYON WALL COLLAPSE
d	Sf. 4 			Continuous seismic event Low-amplitude reflection Distinct wave-shape seismic boundary(2500–5000, Ave. 3500)	BATHYAL FINE GRAINED LAYERS

Fig. 5. Seismic facies based on the integration of seismic-core-log data. Sf.1 to Sf.4 are listed from the top to the bottom (as shown in the row a to d). Columns from the left to the right are: corresponding logging curves, corresponding core samples, seismic interpretations, seismic facies characteristics and their sediment facies. The classification of sediment facies is based on the theory from Posamentier (2003).

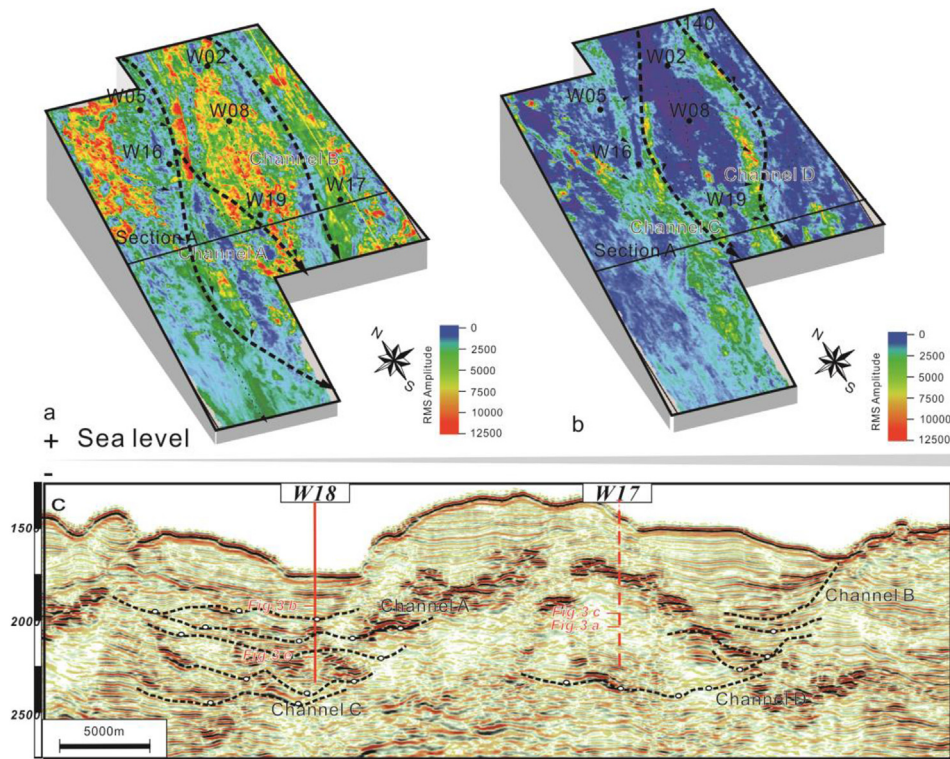


Fig. 6. The distribution of channel deposition (the high RMS zone). (a) and (b) are RMS maps. The upper ones represent the mud turbidity flow distribution during the Wanshan period (Pliocene); the lower ones represent the sandy turbidity flow distribution during the Wanshan period (Late Miocene). (c) is the seismic profile which show the distribution of the channel and their responding evolution.

-grain sediment. Channel D has a similar geometry with Channel C (Fig. 6-b), while its bifurcation points is further than that of Channel C.

Channel A is mainly filled with high density turbidity flow and mass coarse-grained injection. Down along with the slope, Channel A begins to bifurcate into branches at the toe of the slope (Fig. 6-a). Channel B (Type II in Table 2): Channel B is filled with low density turbidity flow with coarse-grained injection as Fig. 3 c shown. Channel B develop down along with the slope with a bifurcation point to the slope break, which located further to slope break than its of Channel A (Fig. 6-a).

As the core section (Fig. 3) shown, the coarse-grained inject the turbidity flow and influence its flow pattern. **From Channel C to Channel A**, Channel C develop more branches and bifurcation points; **From Channel D to Channel B**, Channel D keep the similar flow pattern.

6. The insight of hydrodynamic numerical simulations

The numerical simulation (Fig. 7-a to c) give a consistent observation that the distribution of two kinds of turbidity flow with different density may be different. Galloway (1998) suggested that the initial density difference and the size variation progress may lead to the discrepancy of width/length ratio, sinuosity ratio, and levee stability of different density turbidity flow. The deposition morphology characterization for two types of turbidity flow is discussed as follows:

6.1. Types of turbidity flows with coarse grain injection

6.1.1. Low density flows

At the entrance of channel, the velocity decreases sharply at the

canyon head. It means that the flow is confined within the canyon. Besides, the unstable canyon wall can bring in some coarse-grained injection. The flow momentum also decreases along the slope due to the flattened gradient at the toe of the slope. Thus, the low-density turbidity flow with coarse-grained injection has a higher stream velocity and a lower lateral stream velocity.

The initial density is expected to be $\rho = 1.5 \times 10^3 \text{ kgm}^{-3}$ in this case. During the coarse-grained injection, the stream velocity increases more obviously than the velocity of sandy flow, and the increased amount can be up to 10% higher than that in sandy flow. Meanwhile, with the coarse-grained injection and the mixture flow formation, the lateral velocity also increases (Fig. 7-d). The lateral velocity is high on the inner bank and low on the outer bank (Fig. 7-d).

Combining with the turbidity flow density we can get the turbidites flow rate distribution of the low density turbidity flow with coarse-grained injection (Fig. 7-d). There is no significantly excessive spilling, and most turbidity flow are confined in the canyon.

6.1.2. High-density turbidity flow

The same analyses is applied to the sandy turbidity channel. The velocity vector of coarse grain turbidity flow is presented in Fig. 7-e. At the entrance of the channel, the flow can easily spill over the nearby canyon wall, and the substantially lateral migration can bring in a large amount of coarse silty sand. Further down the stream, with more coarse grain injection, the density and viscosity of the flow also increase. At the bifurcation point, the velocity migrate upward (Fig. 7-c), and more channel branch developed. Compared with the initial flow, the spilling effect and the later density difference lead the flow velocity decrease faster. At the toe of the slope, the slope gradient is flattened, so the flow momentum is also decreased sharply.

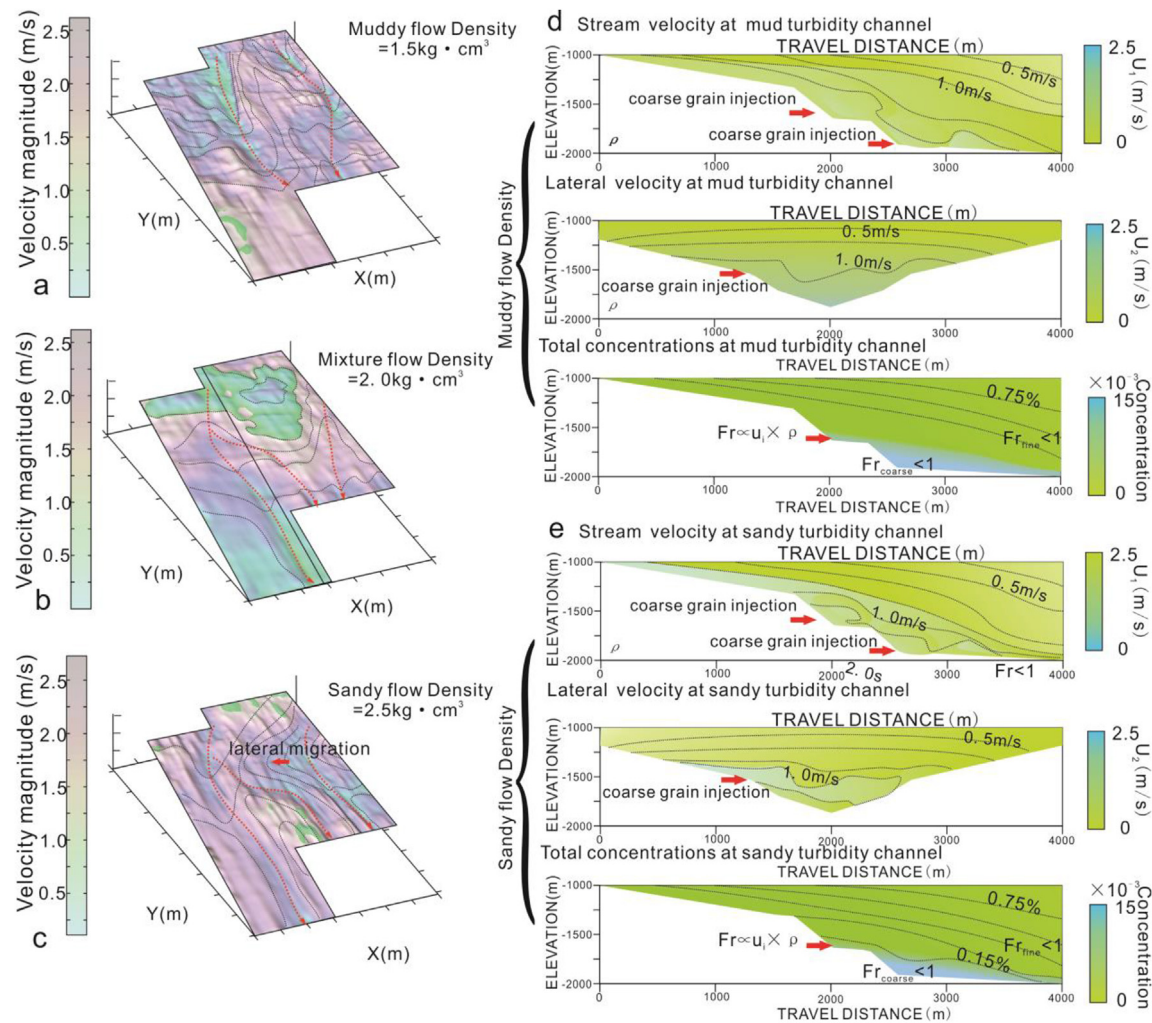


Fig. 7. Velocity (m/s) of different kinds of turbidity flow after 200 s. The sedimentary parameters are selected as shown in Table 1. The initial density is $\rho_0 = 1.5 \times 10^3 \text{ kgm}^{-3}$; the mud flow density is $\rho_0 = 1.5 \times 10^3 \text{ kgm}^{-3}$; the mixture flow density is $\rho_1 = 2.0 \times 10^3 \text{ kgm}^{-3}$; the sandy flow density is $\rho_2 = 2.5 \times 10^3 \text{ kgm}^{-3}$. (a) to (c) is the velocity of corresponding density based on the subcritical turbidity flow model. The base map of velocity chorisogram (a) to (c) is the paleo-geomorphic of 5.5 Ma, 7.5 Ma and 10.5 Ma. Stream velocity, lateral velocity, and the total sediments concentration of different kinds turbidity flow are listed in (d) to (j). (d) and (f) illustrate the sandy flow velocity change during the coarse-grained injection process; (h) and (j) illustrate the mud flow velocity change during the coarse-grained injection process. Different with the turbulence model of Huang et al., (2007), most of the flow in the deep water area is sorting well and can be divided into the high-density part and the low density ones. Different with the turbulence model of Huang et al., (2007), most of the flow in the deep water area is sorting well and can be divided into the high-density part and the low density ones.

Table 2 The corresponding channel type and their sedimentary structure.				
Type no.	Corresponding channel	Initial density	Sedimentary structure	Lithologic sequence modification
Type I	Channel A	Low density	Mixture of the mud turbidity and sandy turbidity, Graded bedding; deformation structure	Mainly mud stone, coarsening-upward; Deformation structure development
Type II	Channel B	Low density	Graded bedding and Wavy bedding	Mainly mud stone, without change
Type III	Channel C	High density	Mixture of the mud turbidity and sandy turbidity, Graded bedding;	Mainly silty stone, coarsening-upward; Deformation structure development
Type IV	Channel D	High density	Graded bedding and Wavy bedding	Mainly silty stone, without change

The stream velocity, the lateral velocity, and the total concentrations at the sandy turbidity channel are presented in Fig. 7-d. The initial density at the entrance of the channel is selected as $\rho = 2.0 \times 10^3 \text{ kgm}^{-3}$, and the injected coarse-grained material is selected as $\Delta\rho = 2.5 \times 10^3 \text{ kgm}^{-3}$. Meanwhile, the stream velocity increases as the coarse grains are injected.

Combining with the turbidity flow density, we can get its turbidites flow rate distribution of the high-density sediments as Fig. 7-e. Therefore, the coarser sediment tends to deposit

unconfined inside, and the turbidity flow can easily spill out and change the nearby slope.

6.2. External impact factors to the flow pattern

According to Picot et al. (2016), both internal and external factors can influence the deposition model. From the perspective of sedimentary sources and supplies, Cecil (2013) pointed out that the sea level is one of the key factors to the turbidity sedimentation.

Besides, [Ercilla et al., \(2002\)](#) also stated that the paleo-geomorphology may influence the formation of the sedimentary gravity flow. However, the two factors (the fluctuating sea levels and the varying topography) can serve as the internal and external factors to influence the subcritical turbidity flow model in the deep-water slope.

The previous studies proposed that the sea levels had an influence on the type of hydrodynamics in the slope break area ([Mulder and Alexander, 2001](#); [Mulder et al., 2006](#), and any others). The fluctuation of the sea level can impact the submarine hydrostatic pressure, which may influence the stability of the submarine deposition. For example, the gas hydrate in the study area of the Baiyun Sag (which was found by GMGS-3 in 2016) is controlled by the pressure. If the sea level fluctuates sharply, it may effuse with the depression of the seabed caused by the sea level regression. And the hydrate effusion may lead to the collapse of the canyon wall and change the later turbidites density.

[Ilstad et al. \(2004\)](#) pointed out that the dip angle of the slope may also play a significant role on the flow pattern and the sedimentary architecture. The long gentle slope may help the turbidity flow run a long distance. It can also be demonstrated in the results from numerical simulation as shown in [Fig. 7-e](#), the velocity of the gravity flow increases with the dip angle of the slope increase. [Ercilla et al. \(2002\)](#) also stated that the syngeneic fault and the canyon wall along the slope play an important role on the flow rate and its lobe distribution.

7. Conclusions

Based on the seismic-log-core data and the quantitative statistical data, we classify the turbidity flow into different types in terms of litho-facies, lithological sequence and the geomorphological characteristics. Besides, we analyze the flow patterns through the method of numerical simulation. Through the flow pattern analysis, the impact factors to the turbidity flow distribution are finally discussed.

There are two major types of turbidity flow based on the difference of the density. After the attribute map analysis, the seismic profile description, and the architecture parameters measurement, we distinguish their difference in terms of the length, erosional capacity, avulsion feasibility, and curvature. The sedimentary characteristics of these turbidity flows are consistent with the sea level circulation.

Combined with the numerical simulation, we calculate the flow rate, erosion rate of different density turbidity flow within the 3-D model. The results show that the coarse-grained high-density flow has a higher vertical erosion rate and a lower lateral abrasion rate. On the other hand, the fine-grained low-density flow has a lower vertical erosion rate and a higher lateral abrasion rate. We reshape the turbidity flow deposition morphology with the help of Fr number, and find that the supercritical turbidity flow ($Fr < 1$) distribution may lead to the discrepancy in different types of turbidity flow.

Acknowledgement

This research was sponsored by the National 127 Project (No.GZ2011003-05-02-02) and National Natural Science Foundation of China (No.41572080), and the Major State Science and Technology Research Program (No. 2016ZX05024002-002). The authors would like to thank Guangzhou Marine Geological Survey for providing the geological and seismic data used for this work. We would also like to express our acknowledgement to the gas hydrate science team of China University of Geoscience (Beijing).

Nomenclature

u_i	the corresponding velocity component of the turbidity flow in the x_i direction
x_1	the direction of turbidity flow along the slope
x_2	the direction along the slope
x_3	the direction of gravity
ρ_n	the density of the turbidity flow
r_n	the grain size of the turbidity flow
P	the overburden pressure
S_{ij}	the average strain-rate tensor
δ_{ij}	Kronecker delta function
N_{mass}	the density mixture ratio
N_{fric}	the vertical erosional capacity

Appendix C. Supplementary data

Supplementary data to this article can be found online at <https://doi.org/10.1016/j.ptlrs.2018.12.001>.

Appendix A

The numerical simulation used the differential equation method based on the finite volume element within non-orthogonal grids ([Ferziger and Peric, 1999](#)). Firstly, the discrete term of Eq. (1) can be regarded as a linear equation. Then, using the fast convergence iterative approach to the linear equations, we get the numerical solutions in each grid:

- 1) Based on the step length and its corresponding density as shown in Table shown and initial velocity(u_i), and introduce the velocity into Eq. (2) and get the result of strain-rate tensor (S_{ij});
- 2) Modify the ultimate velocity with the strain-rate tensor
- 3) Loop the above progress until the convergence of time step;
- 4) Enter into the next step and repeat the above progress.

Appendix B

The numerical method used simulate the coarse-grained injection progress is also based on the finite volume element methods within non-orthogonal:

- 1) Based on the step length and its corresponding density as Table shown and initial velocity (u_i);
- 2) Introduce the velocity into Eq. (2) and get the result of strain-rate tensor (S_{ij});
- 3) Calculate the density mixture ratio(N_{mass})and it responding N_{fric} with Eq. (3) and Eq. (4);
- 4) Introduced the above result into the integral formula (Eq. (5)) and modify the ultimate velocity;
- 5) Loop the above progress until the convergence of time step;
- 6) Enter into the next step and repeat the above progress.

References

- Boulay, S., Colin, C., Trentesaux, A., Frank, N., Liu, Z., 2005. Sediment sources and East Asian monsoon intensity over the last 450 ky. Mineralogical and geochemical investigations on South China Sea sediments. *Palaeogeogr. Palaeoclimatol. Palaeoecol.* 228 (3–4), 260–277.
- Bouma, A.H., Kuenen, P.H., Shepard, F.P., 1962. Sedimentology of some flysch deposits: a graphic approach to facies. Interpretation 6.
- Cecil, C.B., 2013. An overview and interpretation of autocyclic and allocyclic processes and the accumulation of strata during the Pennsylvanian–Permian transition in the central Appalachian Basin, USA. *Int. J. Coal Geol.* 119, 21–31.
- Clift, P.D., Brune, S., Quinteros, J., 2015. Climate changes control offshore crustal

- structure at South China Sea continental margin. *Earth Planet. Sci. Lett.* 420, 66–72.
- Dott, R.H.J., 1963. Dynamics of subaqueous gravity depositional processes. *AAPG (Am. Assoc. Pet. Geol.) Bull.* 47 (1), 104–128.
- El-Gawad, A., Pirmez, C., Cantelli, A., Minisini, D., Sylvester, Z., Imran, J., et al., 2012. 3-D numerical simulation of turbidity currents in submarine canyons off the Niger delta. *Mar. Geol.* 326–328, 55–66.
- Ercilla, G., Alonso, B., Wynn, R.B., Baraza, J., 2002. Turbidity current sediment waves on irregular slopes: observations from the Orinoco sediment–wave field. *Mar. Geol.* 192 (1–3), 171–187.
- Ferziger, J.H., Peric, M., 1999. *Computational Methods for Fluid Dynamics*, 2nd ed. Springer, Berlin.
- Flint, S.S., Hodgson, D.M., Sprague, A.R., Brunt, R.L., Merwe, W.C.V.D., Figueiredo, J., Prélât, A., Box, D., Celma, C.D., Kavanagh, J.P., 2011. Depositional architecture and sequence stratigraphy of the Karoo basin floor to shelf edge succession, Laingsburg depocentre, South Africa. *Mar. Petrol. Geol.* 28, 658–674.
- Galloway, W.E., 1998. Siliciclastic slope and base-of-slope depositional systems: component facies, stratigraphic architecture, and classification. *AAPG (Am. Assoc. Pet. Geol.) Bull.* 82 (4), 287–288.
- Garcia, M., Parker, G., 1993. Experiments on the entrainment of sediment into suspension by a dense bottom current. *J. Geophys. Res. Atmos.* 98 (98), 4793–4808.
- Gardner, M.H., Borer, J.M., Melick, J.J., Mavilla, N., Dechesne, M., Wagerle, R.N., 2003. Stratigraphic process-response model for submarine channels and related features from studies of Permian Brushy Canyon outcrops. *West Texas: Mar. Petrol. Geol.* 20, 757–787.
- Georgoulas, A.N., Kopasakis, K.I., Angelidis, P.B., Kotsovinos, N.E., 2012. Numerical investigation of continuous, high density turbidity currents response, in the variation of fundamental flow controlling parameters. *Comput. Fluid* 60 (10), 21–35.
- Gong, C., Wang, Y., Zheng, R., Hernández-Molina, F.J., Li, Y., Stow, D., Xu, Q., RE, 2016. Middle Miocene reworked turbidites in the Baiyun Sag of the Pearl River Mouth Basin, northern South China sea margin: processes, genesis, and implications. *J. Asian Earth Sci.* 128, 116–129.
- Grachev, A.A., Fairall, C.W., 2001. Upward momentum transfer in the marine boundary layer. *J. Phys. Oceanogr.* 31 (7), 1698–1711.
- Han, J., Xu, G., Li, Y., Zhuo, H., 2016. Evolutionary history and controlling factors of the shelf breaks in the Pearl River Mouth Basin, northern South China sea. *Mar. Petrol. Geol.* 77, 179–189.
- Hodson, J.M., Alexander, J., 2010. The effects of grain-density variation on turbidity currents and some implications for the deposition of carbonate turbidites. *J. Sediment. Res.* 80 (6), 515–528.
- Huang, H., Imran, J., Pirmez, C., 2007. Numerical modeling of poorly sorted depositional turbidity currents. *J. Geophys. Res. Oceans* 112 (112), 141–143.
- Ildstad, T., Marr, J.G., Elverhøi, A., Harbitz, C.B., 2004. Laboratory studies of subaqueous debris flows by measurements of pore-fluid pressure and total stress. *Mar. Geol.* 213 (1–4), 403–414.
- Iverson, R.M., 1997. The physics of debris flows. *Rev. Geophys.* 35 (3), 245–296.
- Iverson, R.M., Lahusen, R.G., 1993. Friction in Debris Flows: Inferences from Large-scale Flume Experiments. *American Society of Civil Engineers*, pp. 1604–1609.
- Kane, I.A., McCaffrey, W.D., Peakall, J., Kneller, B.C., 2010. Submarine channel levee shape and sediment waves from physical experiments. *Sediment. Geol.* 223 (1), 75–85.
- Li, N., Feng, D., Chen, L., Wang, H., Chen, D., 2017. Compositions of foraminifera-rich turbidite sediments from the Shenhu area on the northern slope of the South China Sea: implication for the presence of deep water bottom currents. *J. Asian Earth Sci.* 138, 148–160.
- Lowe, D.R., 1982. Sediment gravity flow II: depositional models with special reference to the deposits of high-density turbidity currents. *J. Sed. Petrol.* 52, 279–297.
- Ma, B., Wu, S., Sun, Q., Mi, L., Wang, Z.Z., Tian, J., 2015. The late cenozoic deep-water channel system in the Baiyun Sag, Pearl River Mouth Basin: development and tectonic effects. *Deep Sea Res. Part II Top. Stud. Oceanogr.* 122, 226–239.
- Marsset, T., Droz, L., Dennielou, B., Pichon, E., 2009. Cycles in the Architecture of the Quaternary Zaire Turbidite System: a Possible Link with Climate. *External Controls on Deep-water Depositional Systems*.
- Milkov, A.V., Sassen, R., 2001. Estimate of gas hydrate resource, northwestern Gulf of Mexico continental slope. *Mar. Geol.* 179 (1), 71–83.
- Mulder, T., Alexander, J., 2001. The physical character of subaqueous sedimentary density flows and their deposits. *Sedimentology* 48 (2), 269–299.
- Mulder, T., Lecroart, P., Hanquiez, V., Marches, E., Gonthier, E., Guedes, J.C., Thiébot, E., Jaïdi, B., Kenyon, N., Voisset, M., 2006. The western part of the Gulf of Cadiz: contour currents and turbidity currents interactions. *Geo Mar. Lett.* 26 (1), 31–41.
- Mutti, E., Tinterri, R., Benevelli, G., Biase, D.D., Cavanna, G., 2003. Deltaic, mixed and turbidite sedimentation of ancient foreland basins. *Mar. Petrol. Geol.* 20, 733–755.
- Nasr-Azadani, M.M., Meiburg, E., 2011. Turbines: an immersed boundary, Navier–Stokes code for the simulation of gravity and turbidity currents interacting with complex topographies. *Comput. Fluid* 45 (1), 14–28.
- Picot, M., Droz, L., Marsset, T., Dennielou, B., Bez, M., 2016. Controls on turbidite sedimentation: insights from a quantitative approach of submarine channel and lobe architecture (Late Quaternary Congo Fan). *Mar. Petrol. Geol.* 72, 423–446.
- Postma, G., Cartigny, M., 2014. Super- and subcritical turbidity currents and their deposits - a synthesis. *Geology* 42 (11), 987–990.
- Postma, G., Kleverlaan, K., Cartigny, M.J.B., 2014. Recognition of cyclic steps in sandy and gravelly turbidite sequences, and consequences for the Bouma facies model. *Sedimentology* 61 (7), 2268–2290.
- Richards, M., 1994. Turbidite systems in deep-water basin margins classified by grain size and feeder system. *AAPG (Am. Assoc. Pet. Geol.) Bull.* 78 (5), 792–822.
- Roberts, M.T., Compani, B., Davis, J.R., Scolman, D.A., 1996. Miocene Example of a Meandering Submarine Channel-levee System from 3-D Seismic Reflection Data. *Gulf of Mexico Basin*, pp. 241–254.
- Salimullah, A.R.M., Stow, D.A.V., 1995. Ichnofacies recognition in turbidites/hemiburidites using enhanced fms images: examples from ODP leg 129. *Log. Anal.* (4).
- Shanmugam, G., Spalding, T.D., Rofheart, D.H., 1993. Process sedimentology and reservoir quality of deep-marine bottom-current reworked sands (sandy contourites): an example from the Gulf of Mexico. *AAPG (Am. Assoc. Pet. Geol.) Bull.* 77 (7), 1241–1259.
- Steinke, S., Groeneveld, J., 2010. East Asian summer monsoon weakening after 7.5Ma: evidence from combined planktonic foraminifera Mg/Ca and $\delta^{18}\text{O}$ (ODP Site 1146; northern South China Sea). *Palaeogeogr. Palaeoclimatol. Palaeoecol.* 289 (4), 33–43.
- Stow, D.A.V., Hernandezmolina, F.J., Llave, E., Sayagogil, M., Diaz, D.R.V., Branson, A., 2009. Bedform-velocity matrix: the estimation of bottom current velocity from bedform observations. *Geology* 37, 327–330.
- Surpless, K.D., Ward, R.B., Graham, S.A., 2009. Evolution and stratigraphic architecture of marine slope gully complexes: monterey Formation (Miocene), Gaviota Beach, California. *Mar. Petrol. Geol.* 26 (2), 269–288.
- Walker, R.G., Harms, J.C., 1970. Thin marine-nonmarine alternations in upper devonian. *AAPG (Am. Assoc. Pet. Geol.) Bull.* 54 (5), 874.
- Wang, X., Lee, M., Collett, T., Yang, S., Guo, Y., Wu, S., 2014. Corrigendum to “Gas hydrate identified in sand-rich inferred sedimentary section using downhole logging and seismic data in Shenhu area, South China Sea”. *Mar. Petrol. Geol.* 54 (2), 141–143.
- Woods, A.W., Bursik, M.I., 1994. A laboratory study of ash flows. *J. Geophys. Res. Solid Earth* 99 (B3), 4375–4394.
- Wu, N., Zhang, H., Yang, S., Zhang, G., Liang, J., Lu, J., Su, X., Schultheiss, P., Holland, M., Zhu, Y., 2011. Gas hydrate system of Shenhu area, northern South China sea: geochemical results. *J. Geol. Res.* 2011, 1687–8833.
- Xie, H., Zhou, D., Li, Y., Pang, X., Li, P., Chen, G., Li, F., Cao, J., 2014. Cenozoic tectonic subsidence in deepwater sags in the Pearl River Mouth Basin, northern South China sea. *Tectonophysics* 615–616, 182–198.
- Zhou, W., Wang, Y., Gao, X., Zhu, W., Xu, Q., Xu, S., Cao, J., Wu, J., 2015. Architecture, evolution history and controlling factors of the Baiyun submarine canyon system from the middle Miocene to quaternary in the Pearl River Mouth Basin, northern South China sea. *Mar. Petrol. Geol.* 67, 389–407.